Surface telluride phases on Pt(111): Reconstructive formation of unusual adsorption sites and well-ordered domain walls

Tilman Kißlinger, Alexandra Schewski ⬤, Andreas Raabgrund ⬤, Hannah Loh ⬤,
Lutz Hammer ⬤,* and M. Alexander Schneider ⬤†

Solid State Physics, Friedrich-Alexander-Universität Erlangen-Nürnberg, Staudtstraße 7, 91058 Erlangen, Germany

For the production of transition-metal dichalcogenides by molecular beam epitaxy, an understanding of the interaction between chalcogenide atoms and metal surfaces is of fundamental interest. Here, we describe the occurrence of stable surface telluride phases when reacting submonolayer amounts of tellurium with a Pt(111) surface. We find that when approaching a Te amount of 0.44 monolayers from below, a disordered Te adsorbate phase is converted into a long-range ordered Pt(111)-(3×3)-4Te surface telluride, which is stable against loss of Te up to 890 K. Adding further Te, heavy domain walls develop that condense into a well-ordered domain structure with (10×10) periodicity. It hosts 49 Te atoms per unit cell and is thermally stable up to 770 K. These two phases are the only existing Te-induced surface reconstructions in the submonolayer regime. The atomic structure of the two phases is determined using low-energy electron diffraction intensity analysis, scanning tunneling microscopy, and density functional theory. The resulting complex surface structures are revealed with picometer accuracy and a great agreement between the employed methods. In particular, the analysis of the (10×10) structure demonstrates the currently achievable state-of-the-art for low-energy electron diffraction structural analyses in terms of experimental surface preparation and data collection but also of computational methods, and it leads the way to building up a structural database for two-dimensional materials and their interfaces.

I. INTRODUCTION

In the wake of graphene, the research of two-dimensional materials has found considerable interest. Among these, transition-metal dichalcogenides (TMDCs) of the form MX_2 (M = metal, X = S, Se, Te) attracted special attention mostly due to their topological properties but also from an application point of view. Platinum-based TMDCs are no exception. In the following, we restrict the references to the system Pt-Te, which is the focus of our study. A broader overview may be obtained from various review articles [1–3]. Apart from the metal to semiconductor transition of $PtTe_2$ in the single-layer limit [4–6] and the observation of a Dirac type-II band structure [7,8], a high activity towards the hydrogen evolution reaction was experimentally observed [9–13]. To investigate this interesting material, one can use single crystals grown by conventional methods, whereby few- or single-layer properties become accessible through exfoliation techniques. These are, however, not applicable for wafer scale production of devices, which calls for physical vapor deposition or molecular beam epitaxy (MBE) processes. While the growth on inert substrates like graphene has been demonstrated [14,15], the Pt-Te system in particular requires a strict control of the Pt-Te ratio as the monotelluride Pt_2Te_2 may occur instead of $PtTe_2$ [16]. Therefore, independent proof of the true crystal structure of the specimen under investigation is indispensable. This is even more important if samples are created by tellurization of Pt films [17,18] or crystal surfaces [19] since here the reservoir of Pt atoms is inexhaustible.

To understand the processes involved, we investigated the tellurization of Pt(111) in the submonolayer regime. We employed low-energy electron diffraction (LEED) using intensity information (LEED-IV) for a determination of the atomic structure of the near-surface region of Pt(111). Scanning tunneling microscopy (STM) and density functional theory (DFT) calculations were used to facilitate the search among possible surface structures and finally to validate the LEED-IV analysis. This allowed us to identify the (3×3) superstructure, which was claimed to be a defective $PtTe_2$ layer [19], as a reconstructed Pt-Te surface telluride. Furthermore, our study shows that the growth of a $PtTe_2$ layer on a bare Pt surface is not possible by tellurization. We think that this is a general observation and may be applicable for other systems where the creation of TMDC layers on the bare substrate was claimed. For such a growth mode, a rather peculiar M-Te interaction would have to be assumed which—during growth—favors the formation of M-Te bonds with M atoms extracted from the surface rather than with those remaining in the surface.

II. METHODS

In our study, two independent ultrahigh-vacuum (UHV) chambers operating at $p < 2 \times 10^{-10}$ mbar and two Pt(111)

---

*lutz.hammer@fau.de
†alexander.schneider@fau.de

crystals cleaned by cycles of Ne^+ sputtering and annealing ($T = 1200–1300$ K) were used. Both vacuum systems were equipped with an ErLEED-type LEED optics [20]. Additionally, the first system housed a room-temperature STM and a sample stage on which the normal incidence of the electron beam on the liquid-nitrogen cooled sample could be adjusted to better than $0.2°$, while the second one was equipped with an STM operating at 78 K. The bias voltage is defined here as the potential of the sample with respect to the tip.

The Te deposition was carried out at sample temperatures ranging from 90 to 350 K without a noticeable difference in the resulting surface structure after annealing. We found that deviations as small as 0.01 ML from the nominal Te coverage of the ordered phases led to the occurrence of easily detectable characteristic satellite spots in LEED. The (3×3) and (10×10) structures reported in this paper are stable up to temperatures of 890 and 770 K, respectively, before Te desorbs.

In the work presented here, we used the newly developed VIPERLEED package [21], which provides a sophisticated tool for LEED-IV data acquisition and manages a modified and parallelized TENSERLEED code [22] for full-dynamical calculation of intensity spectra and parameter fitting. Experimental LEED-IV data were recorded at normal incidence by a cooled 12-bit CCD camera in steps of 0.5 eV for energies up to 680 eV or 400 eV, for the (3×3) and (10×10) structure respectively. The data was stored for off-line evaluation. Energy-dependent variations in the detection device (LEED-optics and camera) were corrected by dividing the dark-field corrected LEED data set by a so called "flat field video." This was obtained by recording the diffuse intensity at the same electron energies as the LEED-IV data from a polycrystalline, nonpolished tungsten ring that is part of the sample holder. Residual noise in the IV-spectra was removed by smoothing the data with a modified Savitzky-Golay filter of 3–5 eV width [23]. Finally, the spectra were inspected manually, and data from energy intervals where the automatic determination of the background intensity obviously failed (e.g., due to a neighboring reflex closeby) or where the intensities were too low to remove the noise by the above-mentioned smoothing routine were discarded. In the case of the (10×10) phase, three independently created IV data sets were averaged for further noise reduction.

The full-dynamical LEED calculations were performed on either 16- or 36-core workstations. For the (10×10) phase, the calculation of full-dynamical reference spectra and tensors required about 25 GB memory per core. Therefore, parallelization was limited by the available memory of 256 GB to 10 cores only, leading to a total calculation time of about 35 h (energy interval 100–400 eV). In comparison, the (3×3) phase required less than 1 GB per core and a total calculation time of about half an hour on 16 cores (100–680 eV). Parameter optimization was performed using the TensorLEED approximation [24], which was a matter of minutes to hours in both cases. Within the model calculations, the lattice parameter for Pt at 90 K was set to 2.770 Å [25] and the respective bulk vibrational amplitude to 0.065 Å, according to a Debye temperature of $\Theta_D = 240$ K [26]. The agreement between model intensities and experimental IV curves was quantified

using Pendry's *R*-factor [27]. Because of the known improper treatment of spin-orbit coupling for heavy elements like Pt in present LEED codes, we neglected electron energies below 100 eV in the analysis as suggested by Materer *et al.* [28]. Our general strategy to tackle such complex systems by LEED is described in detail in the Appendix.

Density functional theory (DFT) calculations were done with the Vienna *Ab-initio* Simulation Package (VASP) [29] using the PBE-PAW general gradient approximation [30] with an energy cutoff of 300 eV with a $6 \times 6 \times 1$ Γ-centered k-point mesh for the (3×3) cell. Calculations of the (10×10) structure were performed at the Γ-point only. For the DFT calculations, the lattice constant of Pt (2.810 Å) was taken from a fully relaxed bulk structure calculation. For comparison with the LEED structure, it was rescaled to the experimental value (2.770 Å). For the (3×3) slabs, six complete Pt(111) layers were set up, of which the three lowest were held fixed at bulk positions during the relaxation. The (10×10) slab was set up with four complete Pt(111) layers of which the two lowest were kept fixed. On both slabs the Te-Pt containing telluride layer was added and the repeated images of the slabs were separated by 14 Å vacuum. The structures were relaxed until forces were smaller than 0.01 eV/Å. STM images were simulated using the Tersoff-Hamann approximation [31].

III. RESULTS AND DISCUSSION

A. The (3×3) phase

When a Te amount below $\Theta_{Te} = 0.4$ ML is deposited on Pt(111) and annealed, a poorly ordered $(\sqrt{3} \times \sqrt{3})R30°$ superstructure is detected that coexists with a (3×3) phase described in the following. From the appearance of the $(\sqrt{3} \times \sqrt{3})R30°$ phase in STM (an example is shown in the SM [32]), we propose that the $(\sqrt{3} \times \sqrt{3})R30°$ surface areas are just a simple Te adsorbate structure representing the densest lattice-gas phase. The first true surface phase that is stable up to annealing temperatures of 890 K is a (3×3) that covers the whole surface at $\Theta_{Te} = 0.44$ ML [Fig. 1], i.e., there must be four Te atoms within the (3×3) unit cell. This precise Te amount was inferred from the calibration using the surface telluride phases on Cu(111) investigated previously [33,34] and by determining the ratio of $(\sqrt{3} \times \sqrt{3})R30°$ and (3×3) covered areas using STM. The reader should note that in the former phase, the Te atoms can be counted directly in atomically resolved STM images, cf. Fig. S1(b) in the SM [32], and thus they give an unambiguous internal fixed point for the coverage. The thus-determined Te coverage of $\Theta_{Te} = 0.44$ ML is conclusively confirmed by the structural LEED-IV analysis below. Experimentally we find an extremely well-ordered surface superstructure exhibiting sharp and low-background intensity LEED images [Fig. 1(a)]. STM images show an extremely regular pattern even at substrate step edges indicating step restructuring during growth. If the Te coverage is tuned carefully, only very few domain boundaries are found [Fig. 1(b)]. For all investigated bias voltages $U_B \leqslant 1$ V, atomically resolved STM images reveal only three protrusions per (3×3) unit cell which form a kagome lattice [Fig. 1(c)]. Assuming that these protrusions correspond to Te atoms, like for many other systems, this indicates that the unit cell contains
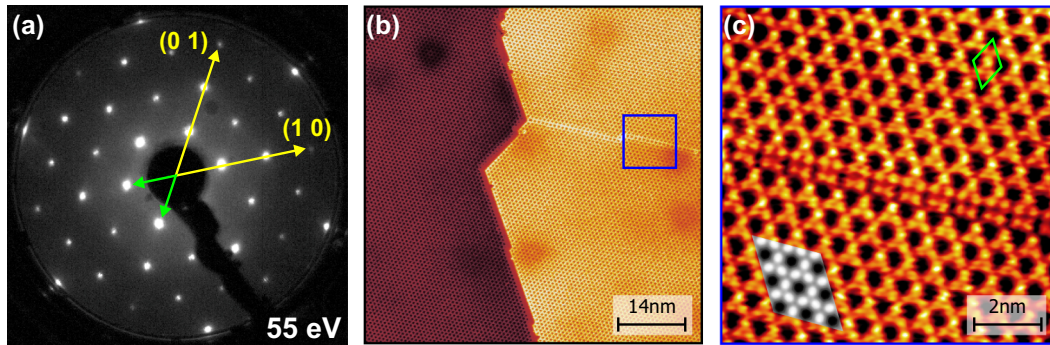
FIG. 1. LEED pattern and corresponding STM images for a Te coverage of $\frac{4}{9}$ ML after subsequent annealing to 890 K. (a) Sharp and low-background (3×3) LEED pattern (55 eV) showing a high degree of lateral order at the surface. (b) Large scale $(70 \text{ nm})^2$ STM image demonstrating that the (3×3) phase expands all over the surface. (c) Zoom into the blue region marked in (b). Atomically resolved $(10 \text{ nm})^2$ STM image with the (3×3) unit cell marked in green. In the middle, a domain boundary can be seen. In the lower left is an overlaid DFT simulated gray scale image using the model of Fig. 2. For details, see the main text. Imaging parameters: (b) $U = 0.4 \text{ V}$, $I = 0.25 \text{ nA}$; (c) $U = 1.0 \text{ V}$, $I = 0.25 \text{ nA}$.

one more Te atom which is invisible to STM. We note that the STM images agree perfectly with the one shown by Liu *et al.* [19] which was claimed to be a defective, (2×2) reconstructed $PtTe_2$ layer. Hence, we prepared the identical system but the interpretation in Ref. [19] is likely incorrect as such a layer would require 0.78 ML of Te. On the contrary, at Te coverages around 0.8 ML, necessary for the claimed defective ditelluride layer, we do not observe any homogeneous phase; cf. Fig. S1(c) in the SM [32].

The appearance in STM and the "missing Te atom" immediately suggest that the (3×3) cannot be a simple adsorbate structure but entails massive reconstructions of the substrate. To reveal the true crystallographic structure of this phase, we carried out a high quality LEED-IV analysis based on as much as 53 symmetrically inequivalent reflexes with a cumulated energy width of $\Delta E = 17.2 \text{ keV}$. The search for suitable models was very effectively supported by DFT relaxations in combination with STM image simulations. All reasonable structural models (presented in the Appendix) led to R-factor values above $R = 0.70$ except the best-fit model discussed in the following. Also, and in particular, the model suggested by Liu *et al.* [19] produced an unsatisfactory fit to the LEED data with an R-factor of $R = 0.82$.

The resulting best-fit model of the structural analysis reproduces the measured LEED-IV spectra with an excellent, overall Pendry R-factor of $R = 0.137$, though below 200 eV the spectra are less well reproduced, probably due to neglecting spin-dependent scattering phase shifts ($R_{\leqslant 200 \text{ eV}} = 0.210$). A ball model of the best-fit structure is depicted in Figs. 2(a) and 2(b). The surface reconstruction is best described as consisting of two layers: In the top layer, three Te atoms are found, adsorbed on fourfold-hollow sites (labeled Te_{4h} in Fig. 2). These adsorption sites are formed by a total of six Pt atoms in either fcc or hcp sites ($Pt_{fcc/hcp}$) in the second layer, which also contains the fourth Te atom. This fourth Te atom (Te_{top}) assumes a very remarkable top site on the Pt layer below. It is thus about 1.2 Å lower than the other three Te_{4h} atoms, which explains why it does not appear in STM images nor in the DFT image simulations, both being largely independent of the tunneling bias.

This configuration is very robust in our structural analysis, e.g., moving the Te one layer down by replacing the Pt atom below it in the third layer would raise the R-factor to $R \approx 0.40$. The Te_{top} atom is characterized by a very short Te-Pt bond length of only 2.53 Å [plus further weak bonds towards the surrounding Pt_{hcp} (2.87 Å) and Pt_{fcc} atoms (3.08 Å)], while the Te_{4h} atoms exhibit larger bond lengths of 2.63–2.65 Å. This may be compared to 2.60 Å in Pt_2Te_2 [35] or 2.68 Å in $PtTe_2$ [36] and show that the Te_{4h} bonds in the surface telluride assume an intermediate character. The lower Pt(111) layers are buckled to a few pm only; a structure file is provided in the SM [32]. Exemplary best-fit LEED-IV spectra to demonstrate the fit quality are shown in Fig. 2(c) and the SM [32]. The huge amount of data ($\Delta E / 4V_{0i} = 801$) allows for the precise determination of 20 structural and 11 nonstructural parameters with a redundancy of $\rho = 25.8$, which is just the amount of data divided by the total number of fitted parameters [37] (for details, see the Appendix). Error analyses of the parameters based on the Pendry R-factor and its variance $\text{var}(R) = 0.0068$ shown in the SM [32] find that the statistical accuracy of the LEED analysis is 1–4 pm for all varied atomic coordinates.

We generally find that the atomic positions of the DFT relaxed structures agree within errors (mean deviation over all fitted parameters: $\approx 2 \text{ pm}$), provided that the DFT Pt lattice parameter is scaled to the experimental value. However, we noticed a peculiar discrepancy around the Te_{top} atom. DFT predicts that the adjacent Pt_{hcp} atoms relax laterally $\approx 8 \text{ pm}$ closer to Te_{top} than determined by LEED-IV, which is far beyond the 2 pm error margin of the LEED analysis. As a consequence, also the Pt atom in the layer below [at position $(0,0)$ of the unit cell in Fig. 2(a)] buckles 8 pm further outwards, leading to the relatively large discrepancy between LEED-IV and DFT in buckling amplitudes of the first unreconstructed Pt(111) layer [Fig. 2(b)]. This strange discrepancy in the relaxation pattern was carefully analyzed by refined DFT calculations including spin-orbit coupling to PBE [38], combining PBE with Grimme D3 vdW [39] correction, using revPBE [40] or PBEsol [41] functionals, or employing the $PBE + U$ approach [42]. None of these functionals could
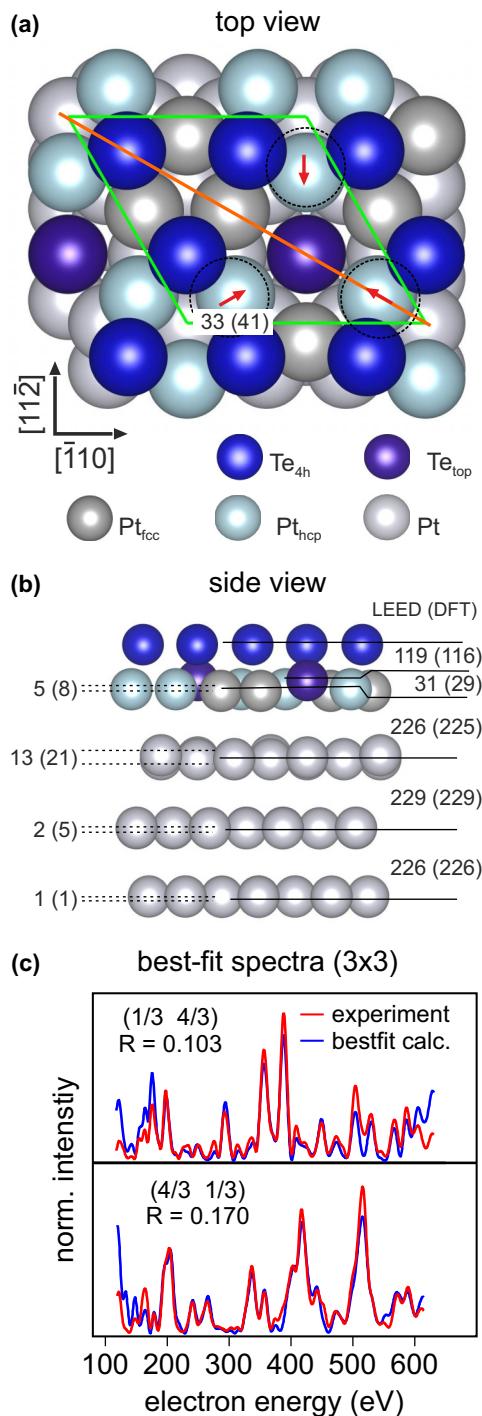
(a) top view

(b) side view

LEED (DFT)

(c) best-fit spectra (3x3)

FIG. 2. Result of the LEED-IV analysis of the Pt(111)-(3 × 3)-4Te phase. (a) Top view. Te is found in fourfold hollow sites (Te$_{4h}$) formed by Pt in fcc and hcp sites and on a top site in the surface Pt layer (Te$_{top}$). There is a significant shift of the Pt$_{hcp}$ from their ideal hcp-hollow positions (marked by red arrows and dashed circles, values in pm, DFT in brackets). (b) Side view along the orange line in (a) (z-scale exaggerated) with relevant (average) layer distances (right) and maximum buckling amplitudes (left) given in pm and compared to the results of a DFT relaxation using standard PBE (in brackets). (c) Two exemplary intensity spectra (out of 53) and comparison with the calculated intensities from the best-fit model. The full set of intensity data and error analysis is provided in the SM [32].

alleviate the discrepancy; only when adding U of the order of 1–2 eV to the Pt d-orbitals could the relaxation pattern of the Pt be improved at the expense of a 10 pm reduction of the bond length between Te$_{4h}$ and Pt$_{fcc/hcp}$, also considerably beyond the positional error margins set by the LEED-IV analysis. Likewise, the coadsorption of hydrogen atoms in the vicinity of the (presumably most reactive) Pt sites close to Te$_{top}$ was tested in calculations on the standard PBE level. However, in these the relaxation pattern of the first-layer Pt atoms changed drastically, again in contradiction to the LEED analysis. With this we want to highlight that structural analyses of the quality presented here may also serve to calibrate and improve theoretical *ab initio* tools to represent structure and bonding configurations.

One might speculate on the mechanisms driving such an uncommon and severe surface reconstruction. From Fig. 2(a) it becomes obvious that the Te atoms assume laterally a perfect hexagonal order, though with a 1.2 Å vertical buckling amplitude of every fourth Te atom. The lateral Te-Te distance corresponds to $1.5a_{Pt} = 4155$ Å. This is not far from the in-plane lattice parameters of PtTe (3.96 Å) and PtTe$_2$ (4.02 Å) [35,43]. This is even better fulfilled for the (10 × 10) phase discussed next, where the average lateral distance ($7/10a_{Pt} = 3.96$ Å) even quantitatively corresponds to the PtTe value. Thus, the interface obviously tries to terminate the crystal towards the vacuum side by a telluride-like Te layer.

However, on the crystal side, the Te layer has to adapt somehow to the substrate's symmetry, lattice parameter, and landscape of the binding potential, which are very case-specific. For an unreconstructed Pt(111) surface, conceivable lateral distances are either by far too small ($1a_{Pt} = 2.77$ Å) or too large ($\sqrt{3}a_{Pt} = 4.80$ Å). Hence, a suitable surface reconstruction is required to offer the correct grid of adsorption sites, whereby even extensive mass transport can be involved due to the utilized high annealing temperatures. In this case, the Pt(111) surface reconstructs into a top layer that is only 2/3 filled. Half of the atoms in that diluted layer are shifted to hcp sites as described above, which offers adsorption sites at the desired distance. In comparison, for Cu(111), where the lateral lattice parameter is significantly smaller (2.55 versus 2.77 Å here), the system instead chooses a half-filled zigzag-like surface reconstruction with $(2\sqrt{3} \times \sqrt{3})R30°$ periodicity, resulting in a pseudohexagonal Te layer with mutual distances of 4.17–4.66 Å [33]. The local binding configuration of Te, on the other hand, seems to be less important, because it is quite different in the two cases. For the Cu(111)-Te phase we found one-sided sixfold coordination towards Cu atoms [33]. In contrast, here in the Pt(111)-(3 × 3)-4Te, we have rather symmetric four- and sevenfold adsorption sites, which deviate only slightly in their binding energies (0.27 eV as determined by DFT). This proves that Te is extremely flexible both in coordination number and bond angles towards substrate atoms, and it allows for very creative and thus quite unpredictable interface structures, which will also make model finding generally laborious.

B. The (10 × 10) phase

Continuing the search for stable surface tellurides, we increased the Te content beyond $\Theta_{Te} = 0.44$ ML. With
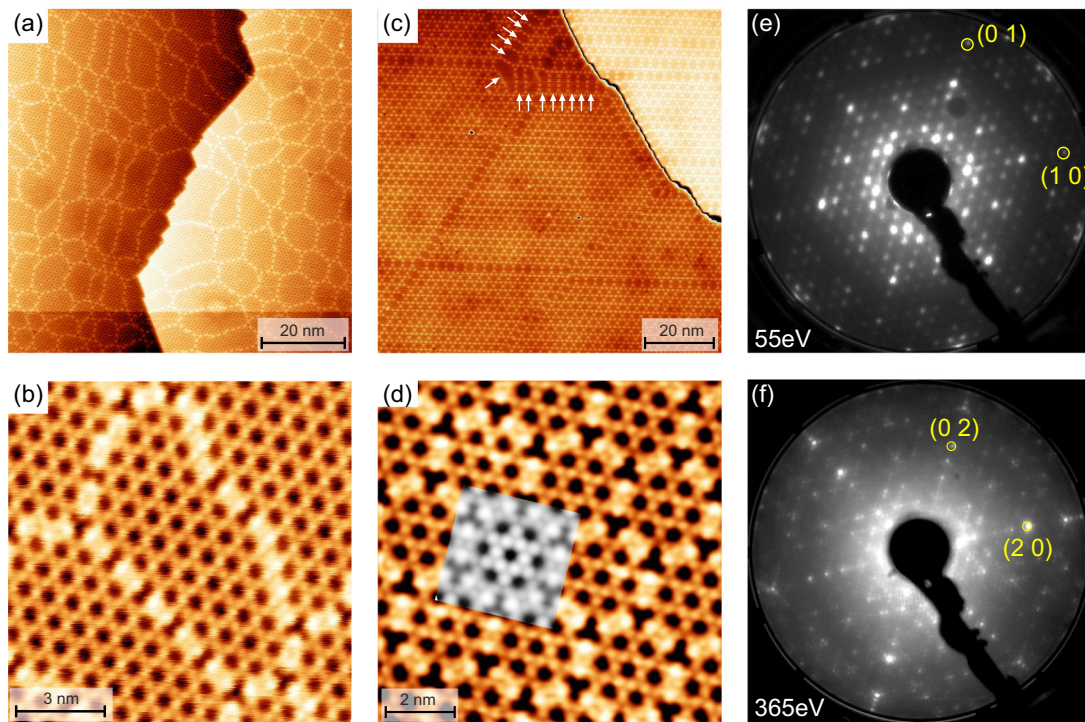
FIG. 3. Formation of the Pt(111)-(10×10)-49Te at Te coverage 0.44 ML $< \Theta_{Te} \leqslant 0.49$ ML imaged by STM (a)–(d) and LEED (e),(f). (a) (3×3) structure with domain boundaries at Θ_{Te} slightly above 0.44 ML. (b) Atomically resolved closeup of the preparation (a). (c) (10×10) structure with remaining (3×3) patches indicated by arrows at Θ_{Te} slightly below 0.49 ML. Note: Each of the bright protrusions in this image corresponds to a pair of threefold-coordinated Te atoms. They also form a kagome-like superlattice. (d) Atomically resolved STM image of the (10×10) and DFT simulated image using the model described in the text. (e),(f) LEED pattern of the surface at $\Theta_{Te} = 0.49$ ML at 55 and 365 eV demonstrating the multitude, density, and in parts quite low intensity of LEED reflexes in the (10×10) phase. (a),(b),(d) Data taken at 300 K, (c) at 78 K, (e),(f) at 90 K. Imaging parameters: (a),(b) $U = 0.15$ V, $I = 0.36$ nA; (c) $U = 0.50$ V, $I = 0.10$ nA; (d) $U = 0.12$ V, $I = 0.75$ nA.

increasing Θ_{Te}, STM images showed a new type of domain boundaries [Fig. 3(a)] characterized by chains of protruding pairs of atoms (presumably Te), which are separated from each other by double depressions [cf. Fig. 3(b)]. At crossing points of the domain boundaries, the latter merge towards triple depressions. The density of such domain boundaries scales with coverage and eventually they develop lateral order with tenfold periodicity with respect to the substrate [Figs. 3(c) and 3(d)]. At $\Theta_{Te} = 0.49$ ML the whole surface is covered by a perfectly ordered (10×10) superstructure [Figs. 3(d)–3(f)], which essentially is a network of (3×3) microdomains consisting of seven unit cells each. The (10×10) superstructure is stable up to temperatures $T < 770$ K. A ball model of the microdomain network is displayed in Fig. 4(a). The domain boundaries between the (3×3) microdomains now just consist of single protruding pairs and triple depressions [cf. Fig. 3(d)], which thus contribute two new structural elements to the (10×10) superstructure. Ball models for these are displayed in Figs. 4(b) and 4(c).

The (10×10) superstructure represents the densest long-range-ordered Te structure on Pt(111) before the growth of compact islands with a hexagonal unit cell ($a_p = 3.96$ Å) sets in with further increasing Te content (see Fig. S1 in [32]). In a forthcoming publication, we will show that the compact islands are in fact platinum monotelluride islands sitting on a Te containing interface, potentially derived from

the (10×10) phase presented here. The continuous evolution from the (3×3) to the (10×10) is reversible upon annealing, allowing for a precise preparation of the Pt(111)-(3×3)-4Te by overdosing Te (≈ 0.5 ML) and annealing in the temperature window $770 < T < 890$ K.

Even though parts of the (10×10) structure must correspond to the previously determined Pt(111)-(3×3)-4Te, the structural analysis of such a large-unit-cell superstructure is a challenge for LEED-IV. To this end, we collected an unprecedentedly large cumulative database of in total $\Delta E = 69.6$ keV consisting of as much as 350 single IV-spectra of independent beams. This allowed us to safely fit the structural model with 170 parameters, while keeping a very high redundancy of $\rho = 17.7$ for the analysis and thus ensuring a high accuracy of determined parameter values.

The collection of data, in particular the automated tracking of spots that are extremely weak in parts [cf. Figs. 3(e) and 3(f)] and setting up the TENSERLEED analysis, would have been impossible without the newly developed VIPER-LEED interface [21]. The included helper programs facilitate both, tracking of LEED beams in the stack of energy dependent images and setting up the possible displacements of the atoms respecting all symmetry constraints of the model. However, we want to emphasize that the computational tools cannot compensate for a careful experimental surface preparation. Only if the structure is extremely long-range ordered,

(a)

(b) **(c)**
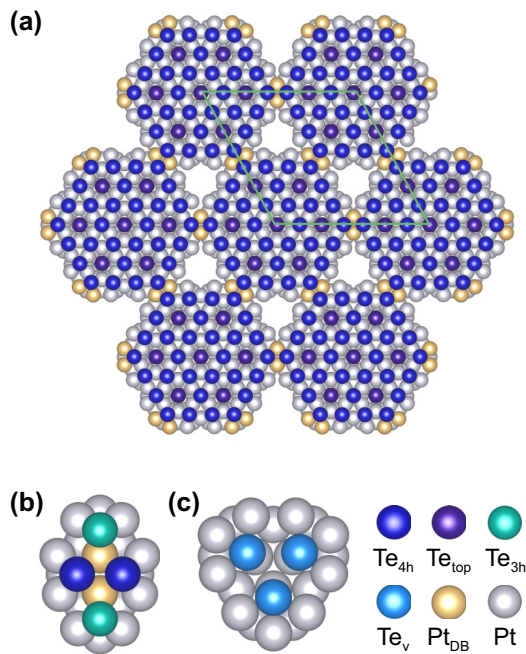
Te$_{4h}$ Te$_{top}$ Te$_{3h}$

Te$_v$ Pt$_{DB}$ Pt

FIG. 4. (a) Visualization of the (10×10) phase as a hexagonally ordered network of corner-sharing (3×3) microdomains consisting of seven unit cells each. At the contact points (domain boundary), the two adjacent fourfold hollow sites share the same two Pt atoms (Pt$_{DB}$). Together with the neighboring Pt-atoms, they form new three-fold hollow sites for Te [Te$_{3h}$, not shown in (a)]. (b) Zoom into a shared microdomain edge. Light green denotes the new threefold bound Te$_{3h}$ species. (c) Zoom into a vacancy island being filled up by three Te$_V$ atoms. They are almost on the top positions of the Pt layer below and attached to two Pt$_{fcc}$ and one Pt$_{hcp}$. (Note: There is a second type of vacancy islands, where the Te$_V$ triple is rotated by $60°$ and attached to one Pt$_{fcc}$ and two Pt$_{hcp}$.)

achieved here by precisely setting the Te content and careful annealing to a temperature just below the onset of Te evaporation, will the LEED reflexes be sufficiently sharp to collect the necessary data for a reliable structure determination.

The search for the best-fit model was guided by the appearance of the surface in STM where (similar to the (3×3)) we assumed bright protrusions to represent Te atoms adsorbed on Pt and we considered dark areas ("holes") being formed by missing Pt atoms in the surface layer. DFT relaxation and STM image simulation helped to sort out unlikely ideas. The final best-fit model is shown in Fig. 5. The reconstructed surface telluride double-layer consists of 49 Te and 66 Pt atoms, whereby the Te atoms are laterally almost equally spaced forming a hexagonal lattice (with (7×7) superstructure) albeit at two distinctly different vertical positions. Over the course of the analysis, all atomic coordinates were fitted within the surface telluride and the first unreconstructed Pt layer (119 parameters). Additionally, vertical displacements for atoms of the next two layers were also adjusted (44 parameters) as well as six vibrational amplitudes for the differently coordinated Pt and Te atoms and a small offset for the inner potential. Other nonstructural parameters were taken from the analysis of the (3×3) phase. All adjusted parameter values
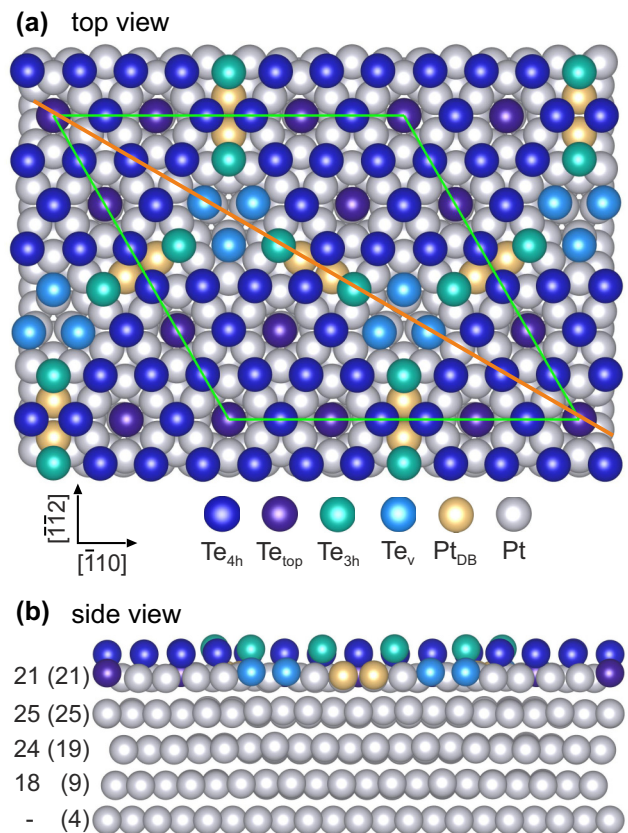
(a) top view

[$\bar{1}\bar{1}2$]
[$\bar{1}10$]

Te$_{4h}$ Te$_{top}$ Te$_{3h}$ Te$_v$ Pt$_{DB}$ Pt

(b) side view

21 (21)
25 (25)
24 (19)
18 (9)
- (4)

FIG. 5. Representation of the best-fit LEED model of the Pt(111)-(10×10)-49Te in the top (a) and side view (b) cut along the orange line in (a). The left side numbers are maximum Pt layer corrugation amplitudes in pm derived by LEED (DFT in brackets).

of the best-fit structure can be taken from the structure data file appended in the SM [32].

The calculated best-fit LEED-IV spectra agree to an overall R-factor of $R = 0.174$ with the experimental spectra. A small selection with single-beam R-factors close to the overall value is shown in Fig. 6(a). The somewhat higher value compared to the analysis of the (3×3) phase is probably due to the larger share of IV data taken at lower energies (<200 eV) within the whole data set. A compilation of all calculated IV spectra is shown in the SM [32] together with their experimental counterparts.

While the atomic coordinates within the microdomains remain largely unchanged compared to the (3×3) phase (except for some slight further relaxations due to the lower local symmetry of most of the sites) the structure of the domain boundaries needs to be discussed in more detail. The protruding pairs of atoms visible in STM are identified as Te atoms (Te$_{3h}$) residing in threefold hollow sites with an adsorption height of about 27 pm above those at the usual fourfold sites (Te$_{4h}$).

The threefold hollow adsorption sites are formed at the contact points of the (3×3) microdomains by three Pt atoms: two regular Pt$_{DB}$ atoms belonging to one of the domains each and one Pt$_{DB}$ atom shared between domains. The adjacent Te$_{4h}$ atoms, displayed in Fig. 4(b), which also appear slightly brighter in STM compared to the other fourfold bound Te
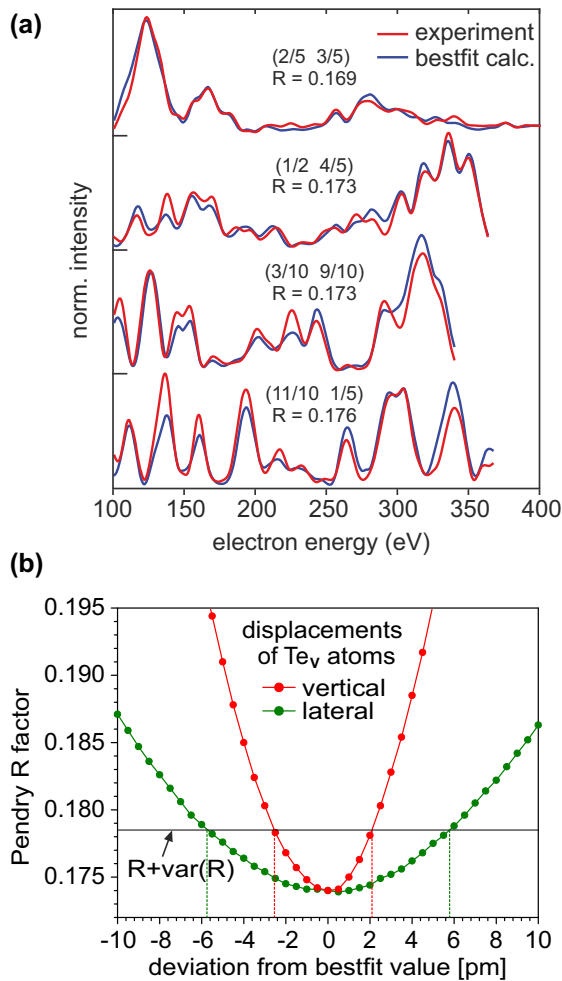
FIG. 6. Representation of the quality and structural sensitivity of the best-fit model for the Pt(111)-(10×10)-49Te phase shown in Fig. 5. (a) Selection of experimental and calculated best-fit IV-spectra (4 out of 350), for which the single beam R-factor corresponds closely to the averaged R-factor. (b) Exemplary error curves for the vertical and lateral positions of the three Te_V atoms resulting from the LEED-IV structural analysis. The vertical dashed lines mark the estimated ranges of uncertainty. The whole collection of IV spectra and error curves is found in the SM.

atoms, are, however, found at equal height with other Te_{4h}. The STM contrast must therefore be purely electronic, presumably caused by a charge redistribution around the (Pt_{DB}) atoms which are the only ones being bound to three instead of two Te atoms. The vacancy islands, which appear in STM as structureless depressions, are found to be filled up by three Te_V atoms residing near the top sites of the underlying closed Pt layer. Their vertical bond has about the same length (2.54 Å) as that of the Te_{top} atoms. The three one-sided in-plane bonds, however, with 2.64–2.72 Å, are significantly shorter than the six lateral bonds of the Te_V, which can be attributed to repulsive forces between the three Te_V atoms within the vacancy island. Also worth mentioning is that the vacancy islands seem to impose quite a severe strain towards the underlying substrate leading to a substantial deep-going and long-range rumpling of the layers, cf. Fig. 5(b). For this reason, we had to extend the fit (of vertical parameters) down

to the third unreconstructed Pt layer, still neglecting even deeper layer rumpling detected by DFT.

The R-factor value of $R = 0.174$ achieved for the best-fit in combination with the huge amount of data available allowed for a very reliable determination of the structural parameters of this phase. According to Pendry's suggestion [27] the parameter range around the best-fit value, where the R-factor value stays below the so-called variance level $R + \mathrm{var}(R)$ (here $\mathrm{var}(R) = 0.0045$ is taken as error margin for the respective parameter). As an example, such error curves for one triple of Te_V atoms are shown in Fig. 6(b). For the telluride overlayer, error margins of 2–4 pm in vertical and 4–9 pm in lateral positions are obtained, depending on how many atoms are coupled by symmetry (one, three, or six). For deeper layers, somewhat larger error margins result due to damping of the electron wave field, but they stay with very few exceptions below 10 pm. A complete list of error margins and a compilation of all error curves is also provided in the SM [32]. Beside this error evaluation based on pure statistical arguments, we have also another access to prove the accuracy of determined parameter values, which is the comparison with the respective DFT predictions. Here, we find a remarkably good quantitative agreement with atomic positions. When scaled to the experimental lattice parameter, the DFT coordinates match the values determined by LEED within 2 pm (vertical) or 3 pm (lateral) on average.

It is commonly claimed that for such large unit cells already a mediocre R-factor value of the order of $R = 0.3$ or even above may be called satisfying. The justification for such statements is that the inherent complexity of those systems quite often does not allow to adjust more than the most relevant parameters, while other smaller displacements have to be ignored in the fit. However, this is a dangerous conjecture, since the contribution of single atoms will have much lower impact to the total outgoing wavefield than for a smaller system. Hence, for a unit cell as large as the present one, even an R-factor value below $R = 0.2$ is no safe proof that the best-fit model is indeed correct in all details, i.e., even single atoms might be missing or incorrectly present in the unit cell. Test calculations showed that, e.g., the addition of an extra Pt atom within each of the vacancy islands (where STM gives no hint about the atomic occupation at all) will raise the R-factor by no more than about $\Delta R = 0.06$. So, there would be room for an improvement of that magnitude as well. We also tested by means of chemical TensorLEED [44] whether all atoms of the present model are needed to explain the experimental data, which was definitively the case. This is also corroborated by the clear parabolic shape of the error curves for all atoms, while nonexisting atoms can typically be shifted anywhere in a fit without affecting the R-factor markedly. However, there is another argument that our structural model is indeed correct and complete, which is the perfect match to the DFT predictions: Any additional or missing atom will have a chemical impact on its local environment and will lead to substantial atomic shifts due to relaxation. If such atoms (or vacancies) are not included in the fitted model, the LEED analysis would still detect the true positions of the remaining atoms. In contrast, DFT would adapt the atomic relaxations to the (erroneous) configuration of the model. On the contrary, one could argue that an unsatisfying correspondence of LEED

and DFT coordinates can be taken as a good indication that the structural model under investigation is at least incomplete.

IV. SUMMARY

In this study, we determined the atomic structure of two well-ordered surface telluride phases on Pt(111) at sub-monolayer Te coverage, namely Pt(111)-(3 × 3)-4Te and Pt(111)-(10 × 10)-49Te. The former was previously identified as a PtTe₂ monolayer, which we prove wrong with our LEED-IV structural analysis. The (10 × 10) turns out to be an ordered arrangement of (3 × 3) microdomains and is among the largest systems ever tackled by a LEED analysis. It was solved with unprecedented accuracy. The analyses show that Te induces a massive rearrangement and partial removal of the surface atoms of Pt(111). As a consequence, the majority of Te atoms in the structures assume fourfold hollow sites, normally not available on fcc(111) surfaces. This comes at the expense that some of the surface layer Pt atoms do not reside in their original fcc positions but shift to hcp and even near-bridge sites. Additionally, a remarkable top-site configuration of Te atoms within the reconstructed first Pt layer is found.

The described surface structures give hints as to how the interface of thicker platinum telluride layers to the Pt substrate is formed. Beyond that particular system, corresponding surface structures may quite generally have to be considered when aiming at producing single metal-ditelluride layers by tellurizing metal surfaces as part of an MBE process.

APPENDIX: DETAILS OF THE LEED ANALYSES

Here we provide further information about the strategies as well as techniques that were applied during the course of the LEED-IV analyses for both the (3 × 3) and (10 × 10) phases of Te on Pt(111). They may serve as guidelines to perform LEED-IV analyses for complex systems.

1. Database, redundancy, and statistical errors

The database of a LEED-IV analysis is the cumulation of all available IV spectra of symmetrically inequivalent beams. Its size is defined by the total energy width ΔE of all these spectra. All individual spectra are treated with equal weight irrespective of diffraction order or intensity with respect to their noise level.

Due to the limited penetration depth of the electron wave into the surface, any diffraction peak is broadened by a Lorentzian function with a FWHM of $2V_{0i}$, whereby V_{0i} is the optical potential (typically of the order of 5 eV). According to Pendry's suggestion [27], twice this FWHM should be regarded as one piece of independent information. Hence, the number N of independent "data points" within the database is just $N = \Delta E / 4V_{0i}$.

Mathematically, this would allow for the determination of N parameters. However, in reality there must be a substantial degree of overdetermination or *redundancy*, $\rho = N/P$, where P is the number of fitted parameters. Though there are no common standards set in LEED, typical values lie between 5 and 10 and are usually also necessary for a reliable fit.

Also according to Pendry [27], the statistical error of a determined parameter can be (rather conservatively) estimated by the parameter range, within which the corresponding R-factor stays below $R + \mathrm{var}(R)$ with $\mathrm{var}(R) = R\sqrt{2/N} = R\sqrt{8V_{0i}/\Delta E}$. For the determination of error margins of a certain parameter, its value has to be shifted off its best-fit value ("error curves") up to the point where the R-factor reaches the $(R + \mathrm{var}(R))$ level. Though, in principle, the data points of such error curves have to be determined by fitting the remaining $(P-1)$ parameters, this is not feasible in practice. Instead, in almost every case (and also in the present analyses), complete independence of parameters is assumed, so that all other parameters can be held fixed at their best-fit values.

In general, there are several reasons why the database entering a LEED-IV analysis should be as large as possible. A larger database reduces the value of $\mathrm{var}(R)$ and thus the error margins, though only $\propto \sqrt[4]{\Delta E}$ (assuming a parabolic shape of the error curves). More important is that the fitting process becomes more stable since secondary R-factor minima in the parameter hyperspace become shallower and even die out eventually. Also, it is usually not obvious from the very beginning of the fitting procedure how many fit parameters are necessary to describe the surface structure correctly. It depends strongly on the physics/chemistry of the actual system how many atoms assume positions significantly deviating from bulk sites *and* lie within the information depth of LEED (which in turn depends on the maximum electron energy used). The same holds for vibrational parameters, which should be fitted for all surface atoms that have a coordination substantially different from that within the bulk. Finally, the larger the redundancy, the higher is the trustworthiness of the analysis.

However, there are also some constraints. First, unreliable data are worse than no data. At worst they contribute with a partial R-factor of $R = 1$, so that their addition will just increase the best-fit R-factor and with that also the error margins.

Therefore, all IV spectra (or parts of them) with unequal spectral behavior of symmetrically equivalent ones were sorted out, as well as those where noise could not be smoothed without significant broadening of spectral features. Secondly, some approximations made in the theoretical description of electron scattering, like, e.g., the assumption of spherical symmetric scatterers, are increasingly violated when the energy is lowered. As already discussed in the main text, this appears to be particularly severe for heavy elements, so that too low energies should also be sorted out (here $E < 100\,\mathrm{eV}$). Finally, it might happen for very large unit cells like the (10 × 10) that the necessary computational requirements, which increase dramatically with energy, exceed the available capacity. However, in recent years the maximum energy of the analysis was in most cases limited by the measurability of spots rather than the available computer power. For the analysis of the (3 × 3) phase, we obtained from the energy range 100–680 eV a total

database of $\Delta E = 17211$ eV, consisting of nine integer order beams with $\Delta E_{int} = 3738$ eV and 44 fractional order beams with $\Delta E_{frac} = 13473$ eV. For the (10×10) we collected in the range 100–400 eV a total of $\Delta E = 69635$ eV data, consisting of five integer order beams with $\Delta E_{int} = 1438$ eV, and 344 fractional order beams with $\Delta E_{frac} = 68197$ eV. The unusually high share of fractional order beams in the analyses provides us with a particular sensitivity to the details of the superstructures.

2. Tested models for the (3×3) phase

The starting point for the model search in the case of the (3×3) phase was the experimentally determined Te coverage of 0.4 ML, i.e., four Te atoms per unit cell, and the STM appearance of a kagome lattice with three protrusions per unit cell. The latter implicates a mutual atomic distance of $1.5\,a_{Pt}$ between the three visible atoms. The apparent threefold symmetry further requires that these atoms need to be placed upon three differently oriented bridge sites of the substrate. Assuming the fourth Te atom central within the STM void, we end up with a laterally hexagonal arrangement of Te atoms. With these constraints, we constructed a number of different models displayed in Figs. 7(a)–7(k) with variable connection to the substrate. The only pure adatom model displayed in Fig. 7(a) needs to have the fourth Te atom substituted within the underlying Pt layer, otherwise, on a top site, it would stick out above the other Te atoms in contrast to the STM observation. All other models (b)–(k) of Fig. 7 refer to Pt_nTe_4 surface telluride overlayers with $n = 2$ (b),(c), $n = 3$ (d),(e), $n = 4$ (f),(g), or $n = 6$ (h)–(k), whereby in model (h) the kagome pattern is generated by Pt rather than Te atoms. For comparison, Fig. 7(l) displays the $PtTe_2$ model with the top Te vacancy proposed by Liu *et al.* [19], which has a very different Te coverage of $\Theta_{Te} = 0.78$.

The compilation in Fig. 7 comprises many but certainly not all conceivable structural models for a (3×3) structure. We stopped the model variation when having found the correct one. This was judged from the corresponding R-factor values (also given in Fig. 7 for each structural model) resulting from rough fits of vertical parameters only [0.03 Å step width for the overlayer and 0.01 Å for the Pt(111) top layer]. Obviously, wrong model types always end up at R-factor values of $R = 0.7$–0.9. Only the models (j) and (k) exhibit much lower values of $R = 0.42$ and 0.30, indicating that they must contain a lot of truth. The two models only differ by the fact that the "invisible" Te atom either sits in a substitutional site in the first Pt layer (j) or just on top of a Pt first-layer atom (k). The latter model, which finally turned out to be the correct one, is clearly favored by the R-factor already at this stage.

3. Choice of fit parameters for the (3×3) and (10×10) phases and optimization process

The number of structurally independent atomic sites of a model depends on the symmetry and size of the unit cell. These sites as well as lateral displacement directions compatible with symmetry are automatically determined by the ViPErLEED system and indicated in the POSCAR files, which are attached as electronic files [32].
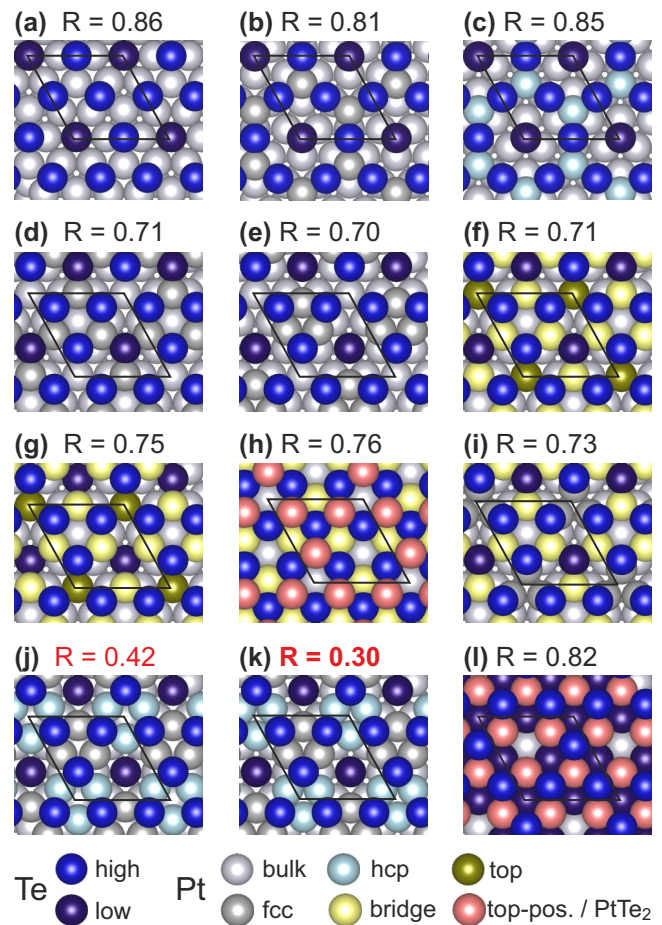

FIG. 7. Structural models for the (3×3) phase of Te/Pt(111) tested during the course of the LEED-IV analysis and corresponding R-factor values obtained after a first rough fit of z parameters. The color code characterizes the Te atoms according to their vertical positions and the Pt atoms essentially according to their lateral position with respect to the underlying bulk layer. (a) Three Te atoms on bridge sites and one substituting a Pt surface atom on the otherwise unreconstructed surface. (b)–(g) Hexagonal arrangement of Te atoms differently linked by either two (b),(c), three (d),(e), or four Pt atoms (f),(g). In (e) and (g), one Te atom substitutes a Pt surface atom. (h) Model with the kagome lattice formed by Pt atoms. (i)–(k) Hexagonal arrangement of Te atoms linked by six Pt atoms at two different sites, whereby the center Te atom sits on a Pt top (i),(k) or substitutional site (j). (l) The $PtTe_2$ model with the top Te vacancy proposed by Liu *et al.* [19] for comparison.

In the case of the best-fit model for the (3×3) phase [Fig. 7(k)], we had to determine three parameters (two vertical and one lateral) for the two different types of Te atoms, and four (a vertical and a lateral one for each type) for the fcc and hcp Pt atoms of the surface telluride. Within the top Pt(111) layer, there are four nonequivalent sites (one of them sixfold-degenerate) within a total of four vertical parameters and one lateral parameter. Because of the rather high energies of up to 680 eV used for the analysis, we also had sufficient sensitivity towards atomic relaxations within deeper layers. Since lateral relaxations turned out to be negligible already within the topmost Pt(111) layer (<0.01 Å), we fitted only vertical positions for the deeper layers. For the second and

third Pt(111) layers these were three parameters each, from which buckling amplitudes of $\leqslant 0.02$ Å resulted. Hence, we treated even deeper-lying layers (fourth and fifth) as rigid and fitted only a possible variation of layer spacings. As expected, the best-fit values ended very close to bulk positions (0.015 and 0.006 Å), further proving the reliability of our fit. Moreover, we also adapted the vibrational amplitudes of the nonequivalent species within the surface telluride and topmost Pt(111) layer, in total eight. As usual for any LEED-IV analysis, there were three additional nonstructural parameters to determine: the optical potential V_{0i}, a small rigid energy offset V_{00} accounting for calibration errors, and an effective polar angle of incidence θ_{eff} in order to mimic the conical shape of the incident beam (fitted to $\theta_{\mathrm{eff}} = 0.51°$). Altogether we had 31 parameters to determine. With a total database of $\Delta E = 17211$ eV and a fitted value of $V_{0i} = 5.37$ eV we have 801 independent pieces of information (cf. Appendix 1) and thus an overdetermination (redundancy) of $\rho = 25.8$.

In the case of the (10×10) phase, we proceeded in an analogous way. As can be seen from the respective POSCAR file, the surface telluride layer with 115 atoms in total (49 Te and 66 Pt) contains only 12 symmetrically nonequivalent Te and 14 Pt sites. This led to 26 independent vertical and 38 lateral parameters (16 for Te and 22 for Pt). The large relative number of lateral parameters compared to the (3×3) phase comes from the fact that only one single atom, the center Te atom of the microdomains, sits on a rotational axis and is thus laterally blocked. Most of the atoms even have two lateral degrees of freedom. The 100 Pt atoms of the first Pt(111) layer divide into 22 symmetrically independent sites leading to another 22 vertical and 33 lateral parameters. The fit of these two layers was completed by the variation of six vibrational amplitudes for classes of structurally similar sites: Te_{top}, Te_{4h}, Te_{3h}, Te_{v}, $Pt_{telluride}$, and Pt_{surf}, leading to as many as 124 fit parameters for these two layers only. Since the lateral relaxations of the topmost Pt(111) layer turned out to be quite small (not unexpected for close-packed layers), we could concentrate in deeper layers on vertical displacements only, which again added another 22 fit parameters per layer. Unfortunately, and different from the (3×3) phase, the buckling amplitudes did not rapidly diminish with depth [cf. Figs. 2(b) and 5(b) of the main text]. For the second and even the third Pt(111) layer, we find an overall corrugation of as much as 0.24 and 0.18 Å, respectively. Disregarding some noise-induced scatter, the corrugation is virtually a long-range wave with maxima at the lateral positions of the vacancy islands, which obviously impose a deep-reaching strain field to the substrate. Figure 8 visualizes these layer corrugations as resulting from the LEED best fit with 10-fold vertical exaggeration.

A neglect of even the third-layer buckling would significantly worsen the overall R-factor value of the LEED fit by about $\Delta R = 0.06$, whereby in particular those spots that are far off from third-order positions in k-space, and hence less affected by the scattering contribution of the (3×3) microdomains, appear to be very sensitive to this buckling. Though the revealed structure would suggest fitting vertical parameters for even deeper layers, we refrained from doing so due to the limited depth sensitivity caused by the quite low maximum energy of our data (400 eV). The error margins for any vertical position determined for a particular site
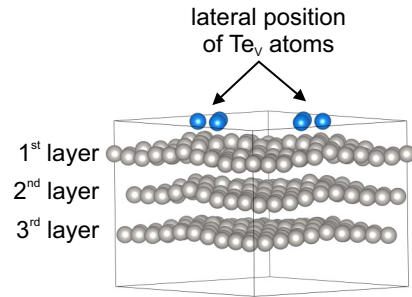

FIG. 8. Visualization of the long-range corrugation of the first three close-packed Pt(111) layers derived from the LEED best-fit structure with 10-fold vertical exaggeration each. Also displayed are the Te_{V} atoms marking the lateral position of the vacancy islands. Vertical distances between the layers are arbitrary.

would exceed the total buckling amplitude. Instead of fitting single-site displacements, it would be more appropriate here to fit the Fourier components of the corrugation, an approach that has already been successfully performed in the case of moire structures, e.g., by Moritz *et al.* [37], but has not been implemented yet in the ViPErLEED routines. To save computational time, we did not fit the effective angle of incidence θ and the optical potential V_{0i} here, but used the corresponding values from the (3×3) analysis adapted to the reduced data energy range ($V_{0i} = 5.80$ eV).

So, we ended up with 170 independent parameters to be determined during the course of the analysis. However, with the enormous database of 69 635 eV available, this was easily achievable with a still high redundancy factor of 17.7.

For both phases, the structural optimization was performed in a stepwise fashion, since the search algorithm implemented in the TensErLEED code only allows for fitting one spatial direction per site (on a defined grid) at the same time. Therefore, we sequentially optimized vertical and lateral parameters, the latter when necessary in two steps, as well as vibrational amplitudes. We performed several of these cycles with decreasing grid increments, which in the case of the (3×3) structure were finally as small as 0.002 Å for vertical and 0.003 Å for lateral and vibrational variations. Due to the lower sensitivity for single-site parameters, larger steps of 0.003–0.005 Å (vertical and vibrational) and 0.005–0.01 Å (lateral) were taken for the finest fit of the (10×10) structure.

4. Sensitivity of the fit towards model and parameter variation

As discussed in Appendix 1 the margins for the *statistical* uncertainty of parameter values can be determined from so-called error curves. For all structural and vibrational parameters varied during the course of both analyses, we have plotted these curves together with the error margins and appended the collections as Supplemental Material (SM) [32]. Of course, the sensitivity, i.e., the curvature of the error curves, and thus also the size of the error margins, depends on the relative contribution of the scattering of the related site to the total scattering amplitude of the model surface. In both phases there are sites consisting of one, three, or six symmetry-equivalent atoms. Hence, the accuracy with which the related parameter

values can be determined differs correspondingly. Also, the relative share of such an atom group is much higher in the case of the (3×3) than the (10×10) phase. And finally, due to normal incidence of the electron beam, the sensitivity is about twice as large for vertical compared to lateral displacements, and it also decreases with the depth of the scatterers below the surface, cf. Fig. 6(b).

A completely different question, however, concerns the certainty about the correctness of the principal model, for which the structural optimization was performed. For rather small unit cells, where every single atom has a significant contribution to the total wave field, its existence (or nonexistence) within the model will have a considerable impact on the R-factor value, at least when fractional site occupancy is unlikely. The same holds for elemental substitution of certain sites, here, e.g., Te by Pt or vice versa, as long as both elements are not too close in the Periodic Table. For comparison, we have repeated the fit for the (3×3) with the best-fit structure modified such that the Te_{top} atom invisible in STM is either removed or substituted by a Pt atom. The corresponding R-factor values amount to $R = 0.248$ and 0.231, respectively, which is almost twice the R-factor value of $R = 0.137$ for our proposed model. Hence, there is hardly a chance that any atom of the model is missing or substituted, at least in the two topmost layers. For deeper layers, there is no physical reason for that. Moreover, additional atoms or vacancies within the model or even a simple elemental exchange will severely influence the relaxation pattern of atoms sitting nearby. This can be analyzed by DFT structural relaxation of the modified model. For example, regarding the above-mentioned Te-Pt exchange, the Pt_{fcc} atoms would laterally shift by 0.23 Å towards the substituted Pt atom, while Pt_{hcp} and Te_{4h} atoms relax mainly inwards by 0.06 and 0.08 Å. And even the underlying Pt(111) layer would suffer vertical atomic relaxations from -0.04 to $+ > 0.12$ Å. In contrast, the LEED fit for the substitution model leaves the coordinates of all these atoms within 0.01 Å at the values of the best-fit model. This may serve as an example of how important the close correspondence of LEED-IV and DFT coordinates is for the trustworthiness of a model.

In the case of the (10×10) structure, the situation is different. Here, the relative scattering contribution of a single atom or even a group of three or six atoms is much smaller compared to (3×3). And the best-fit R-factor value of $R = 0.174$ would still leave some room for improvement. Since the internal structure of the (3×3) microdomains hardly gives a reason for structural variations, we only tested some modifications of the atomic occupation of the vacancy islands, which is already discussed in the main text. Nevertheless, solely from LEED-IV we can hardly state that the proposed model is correct up to the last atom. Here, the observed close correspondence to the structural parameters predicted by DFT (also discussed in the main text) is indeed essential for strong confidence into our model.

---

[1] S. Manzeli, D. Ovchinnikov, D. Pasquier, O. V. Yazyev, and A. Kis, 2D transition metal dichalcogenides, Nat. Rev. Mater. **2**, 17033 (2017).

[2] W. Choi, N. Choudhary, G. H. Han, J. Park, D. Akinwande, and Y. H. Lee, Recent development of two-dimensional transition metal dichalcogenides and their applications, Mater. Today **20**, 116 (2017).

[3] Q. Fu, J. Han, X. Wang, P. Xu, T. Yao, J. Zhong, W. Zhong, S. Liu, T. Gao, Z. Zhang, L. Xu, and B. Song, 2D transition metal dichalcogenides: Design, modulation, and challenges in electrocatalysis, Adv. Mater. **33**, 1907818 (2021).

[4] R. A. B. Villaos, C. P. Crisostomo, Z.-Q. Huang, S.-M. Huang, A. A. B. Padama, M. A. Albao, H. Lin, and F.-C. Chuang, Thickness dependent electronic properties of Pt dichalcogenides, npj 2D Mater. Appl. **3**, 2 (2019).

[5] K. Deng, M. Yan, C.-P. Yu, J. Li, X. Zhou, K. Zhang, Y. Zhao, K. Miyamoto, T. Okuda, W. Duan, Y. Wu, X. Zhong, and S. Zhou, Crossover from 2D metal to 3D Dirac semimetal in metallic PtTe$_2$ films with local Rashba effect, Sci. Bull. **64**, 1044 (2019).

[6] M.-K. Lin, R. A. B. Villaos, J. A. Hlevyack, P. Chen, R.-Y. Liu, C.-H. Hsu, J. Avila, S.-K. Mo, F.-C. Chuang, and T.-C. Chiang, Dimensionality-mediated semimetal-semiconductor transition in ultrathin PtTe$_2$ films, Phys. Rev. Lett. **124**, 036402 (2020).

[7] M. Yan, H. Huang, K. Zhang, E. Wang, W. Yao, K. Deng, G. Wan, H. Zhang, M. Arita, H. Yang, Z. Sun, H. Yao, Y. Wu, S. Fan, W. Duan, and S. Zhou, Lorentz-violating type-II Dirac fermions in transition metal dichalcogenide PtTe$_2$, Nat. Commun. **8**, 257 (2017).

[8] M. S. Bahramy, O. J. Clark, B.-J. Yang, J. Feng, L. Bawden, J. M. Riley, I. Marković, F. Mazzola, V. Sunko, D. Biswas, S. P. Cooil, M. Jorge, J. W. Wells, M. Leandersson, T. Balasubramanian, J. Fujii, I. Vobornik, J. E. Rault, T. K. Kim, M. Hoesch *et al.*, Ubiquitous formation of bulk Dirac cones and topological surface states from a single orbital manifold in transition-metal dichalcogenides, Nat. Mater. **17**, 21 (2018).

[9] D. Kong, J. J. Cha, H. Wang, H. R. Lee, and Y. Cui, First-row transition metal dichalcogenide catalysts for hydrogen evolution reaction, Energy Environ. Sci. **6**, 3553 (2013).

[10] X. Chia, A. Adriano, P. Lazar, Z. Sofer, J. Luxa, and M. Pumera, Layered platinum dichalcogenides (PtS$_2$, PtSe$_2$, and PtTe$_2$) electrocatalysis: Monotonic dependence on the chalcogen size, Adv. Funct. Mater. **26**, 4306 (2016).

[11] S. Lin, Y. Liu, Z. Hu, W. Lu, C. H. Mak, L. Zeng, J. Zhao, Y. Li, F. Yan, Y. H. Tsang *et al.*, Tunable active edge sites in PtSe$_2$ films towards hydrogen evolution reaction, Nano Energy **42**, 26 (2017).

[12] D. Hu, T. Zhao, X. Ping, H. Zheng, L. Xing, X. Liu, J. Zheng, L. Sun, L. Gu, C. Tao *et al.*, Unveiling the layer-dependent catalytic activity of PtSe$_2$ atomic crystals for the hydrogen evolution reaction, Angew. Chem. **131**, 7051 (2019).

[13] Y. Wang, K. Szokolova, M. Z. M. Nasir, Z. Sofer, and M. Pumera, Layered crystalline and amorphous platinum disulfide (PtS$_2$): Contrasting electrochemistry, Chem. Eur. J. **25**, 7330 (2019).

[14] S. Song, I. Oh, S. Jang, A. Yoon, J. Han, Z. Lee, J.-W. Yoo, and S.-Y. Kwon, Air-stable van der Waals PtTe$_2$ conductors with

high current-carrying capacity and strong spin-orbit interaction, iScience **25**, 105346 (2022).

[15] K. Zhang, M. Wang, X. Zhou, Y. Wang, S. Shen, K. Deng, H. Peng, J. Li, X. Lai, L. Zhang, Y. Wu, W. Duan, P. Yu, and S. Zhou, Growth of large scale PtTe, PtTe₂ and PtSe₂ films on a wide range of substrates, Nano Res. **14**, 1663 (2021).

[16] K. Lasek, M. Ghorbani-Asl, V. Pathirage, A. V. Krasheninnikov, and M. Batzill, Controlling stoichiometry in ultrathin van der Waals films: PtTe₂, Pt₂Te₃, Pt₃Te₄, and Pt₂Te₂, ACS Nano **16**, 9908 (2022).

[17] H. Xu, J. Wei, H. Zhou, J. Feng, T. Xu, H. Du, C. He, Y. Huang, J. Zhang, Y. Liu, H.-C. Wu, C. Guo, X. Wang, Y. Guang, H. Wei, Y. Peng, W. Jiang, G. Yu, and X. Han, High Dirac semimetal in large-area type-II Dirac semimetal PtTe₂, Adv. Mater. **32**, 2000513 (2020).

[18] Z. Dong, W. Yu, L. Zhang, L. Yang, L. Huang, Y. Zhang, Z. Ren, H. Mu, C. Chen, J. Zhang, J. Li, L. Wang, and K. Zhang, Wafer-scale patterned growth of type-II Dirac semimetal platinum ditelluride for sensitive room-temperature terahertz photodetection, InfoMat (2023).

[19] L. Liu, D. Zemlyanov, and Y. P. Chen, Epitaxial growth of monolayer PdTe₂ and patterned PtTe₂ by direct tellurization of Pd and Pt surfaces, 2D Mater. **8**, 045033 (2021).

[20] ErLEED150, SPECS Surface Nano Analysis GmbH, Berlin, Germany.

[21] A. Imre, F. Kraushofer, F. Doerr, T. Kisslinger, M. Schmid, U. Diebold, L. Hammer, and M. Riva, ViPErLEED: A modern all-in-one LEED I(V) package, http://hdl.handle.net/20.500.12708/136352 and https://github.com/viperleed.

[22] V. Blum and K. Heinz, Fast LEED intensity calculations for surface crystallography using Tensor LEED, Comput. Phys. Commun. **134**, 392 (2001).

[23] M. Schmid, D. Rath, and U. Diebold, Why and how Savitzky-Golay filters should be replaced, ACS Meas. Sci. Au **2**, 185 (2022).

[24] P. J. Rous, J. B. Pendry, D. K. Saldin, K. Heinz, K. Müller, and N. Bickel, Tensor LEED: A technique for high-speed surface-structure determination, Phys. Rev. Lett. **57**, 2951 (1986).

[25] J. Arblaster, Crystallographic properties of platinum, Platinum Metals Rev. **41**, 12 (1997).

[26] C. Kittel, *Einführung in die Festkörperphysik* (Oldenbourg, Munich, 1980).

[27] J. B. Pendry, Reliability factors for LEED calculations, J. Phys. C **13**, 937 (1980).

[28] N. Materer, U. Starke, A. Barbieri, R. Döll, K. Heinz, M. Van Hove, and G. Somorjai, Reliability of detailed leed structural analyses: Pt(111) and Pt(111)-p(2 × 2)-O, Surf. Sci. **325**, 207 (1995).

[29] G. Kresse and J. Furthmüller, Efficient iterative schemes for *ab initio* total-energy calculations using a plane-wave basis set, Phys. Rev. B **54**, 11169 (1996).

[30] J. P. Perdew, K. Burke, and M. Ernzerhof, Generalized gradient approximation made simple, Phys. Rev. Lett. **77**, 3865 (1996).

[31] J. Tersoff and D. R. Hamann, Theory of the scanning tunneling microscope, Phys. Rev. B **31**, 805 (1985).

[32] See Supplemental Material at http://link.aps.org/supplemental/10.1103/PhysRevB.108.205412 for additional STM results and electronic data files with the results of the structural analyses performed.

[33] T. Kißlinger, A. Raabgrund, B. Geldiyev, M. Ammon, J. Rieger, J. Hauner, L. Hammer, T. Fauster, and M. A. Schneider, CuTe chains on Cu (111) by deposition of one-third of a monolayer of Te: Atomic and electronic structure, Phys. Rev. B **102**, 155422 (2020).

[34] T. Kißlinger, M. A. Schneider, and L. Hammer, Submonolayer copper telluride phase on Cu(111): Ad-chain and trough formation, Phys. Rev. B **104**, 155426 (2021).

[35] K. Cenzual, L. M. Gelato, M. Penzo, and E. Parthé, Overlooked trigonal symmetry in structures reported with monoclinic centred bravais lattices; trigonal description of Li₈Pb₃, PtTe, Pt₃Te₄, Pt₂Te₃, LiFe₆Ge₄, LiFe₆Ge₅, CaGa₆Te₁0 and La₃.₂₆₆Mn₁.₁₅₆, Z. Kristallogr. **193**, 217 (1990).

[36] S. Furuseth, K. Selte, A. Kjekshus, S. Gronowitz, R. A. Hoffman, and A. Westerdahl, Redetermined crystal structures of NiTe₂, PdTe₂, PtS₂, PtSe₂, and PtTe₂, Acta Chem. Scand. **19**, 257 (1965).

[37] W. Moritz, B. Wang, M.-L. Bocquet, T. Brugger, T. Greber, J. Wintterlin, and S. Günther, Structure determination of the coincidence phase of graphene on Ru(0001), Phys. Rev. Lett. **104**, 136102 (2010).

[38] S. Steiner, S. Khmelevskyi, M. Marsmann, and G. Kresse, Calculation of the magnetic anisotropy with projected-augmented-wave methodology and the case study of disordered Fe₁₋ₓCoₓ alloys, Phys. Rev. B **93**, 224425 (2016).

[39] S. Grimme, J. Antony, S. Ehrlich, and H. Krieg, A consistent and accurate *ab initio* parametrization of density functional dispersion correction (DFT-D) for the 94 elements H–Pu, J. Chem. Phys. **132**, 154104 (2010).

[40] Y. Zhang and W. Yang, Comment on "generalized gradient approximation made simple," Phys. Rev. Lett. **80**, 890 (1998).

[41] J. P. Perdew, A. Ruzsinszky, G. I. Csonka, O. A. Vydrov, G. E. Scuseria, L. A. Constantin, X. Zhou, and K. Burke, Restoring the density-gradient expansion for exchange in solids and surfaces, Phys. Rev. Lett. **100**, 136406 (2008).

[42] S. L. Dudarev, G. A. Botton, S. Y. Savrasov, C. J. Humphreys, and A. P. Sutton, Electron-energy-loss spectra and the structural stability of nickel oxide: An LSDA+U study, Phys. Rev. B **57**, 1505 (1998).

[43] S. Bhan, T. Gödecke, and K. Schubert, Konstitution einiger Mischungen des Platins mit b-Elementen (B = Sn, Sb, Te), J. Less-Common Met. **19**, 121 (1969).

[44] R. Döll, M. Kottcke, and K. Heinz, Chemical substitution of surface atoms in structure determination by tensor low-energy electron diffraction, Phys. Rev. B **48**, 1973 (1993).